

# LEFT VENTRICLE'S SURFACE RECONSTRUCTION AND VOLUME ESTIMATION

O. García  
CITEM

EA La Salle / Universitat Ramon Llull  
C/ Quatre Camins 2, 08022 Barcelona  
oscarg@salleURL.edu

A. Susín

Departament de Matemàtica Aplicada I  
Universitat Politècnica de Catalunya  
Avda. Diagonal 647, 08028 Barcelona  
toni.susin@upc.es

## Abstract

*This document describes the three-dimensional reconstruction of the internal and external surfaces of the human's left ventricle from actual SPECT data. The reconstruction is a first process fitting in a complete VR application that will serve as an important diagnosis tool for hospitals. Beginning with the surfaces reconstruction, the application will provide volume and interactive real-time manipulation to the model. We focus on speed, precision and smoothness for the final surfaces. As long as heart diseases diagnosis requires experience, time and professional knowledge, simulation is a key-process that enlarges efficiency.*

## Keywords

*Tele-medicine, deformable models, virtual reality, image processing, 3D surface reconstruction.*

## 1. INTRODUCTION

Access to a 3D model obtained from patient's data can have several applications like support on diagnosis, surgery planning, student's training or even remote-operation. A first approximation to the problem would be using a manual process with specific image-processing software [Quackenbush96] though it would require deep medical knowledge and experience.

Some parts of the human body like skin or bones have clear intensity-gradient variations that make surface-reconstruction techniques, like the Marching Cubes [Lorensen87], suitable. Unfortunately these techniques don't work when regions are formed from soft tissue. That's the case of the heart, liver or muscles.

In order to solve those cases several contour-based techniques have been introduced: Snakes [Kass88], Active Nets [Sakaue96], 3D Active Nets [Takanashi98] and Active Cubes [Bro-Nielsen94]. In all the approximations the evolution is similar, an initial parametrically defined contour or mesh which deforms attracted to a certain energy minima, numerically implemented as a finite-differences method.

Another possible approach is to use the Finite Element methods [Cohen93][McInerney94]. Those methods give nice results but are computationally expensive and complex.

The dynamic model that we present solves the same type of problems using the evolution of a deformable mesh affected by internal and external forces. Internal forces are defined in terms of elasticity; external forces are derived from the data set as a vector field called GVF [Xu97][Xu98].

The use of the GVF vector field avoids some of the limitations of traditional snakes related to initial distance to data and robustness in concave regions.

## 2. INPUT DATA

The system takes as its input SPECT, Single Photon Emission Computed Tomography, images. Those images give functionality keys about the organ and do not describe its anatomy. Thus data shows the activity being held in terms of the amount of useful tissue, without giving a clue about shape. From this knowledge it becomes clear that ischemic areas, it means in absence of blood irrigation, won't be shown in the images. That's the case of ventricle areas being affected by a heart attack.

SPECT data samples are shown in figure 1.

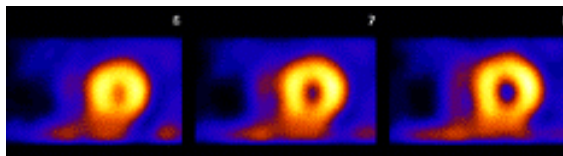


Figure 1: SPECT imagery [Mannting95].

Two of the main diagnosis parameters of interest for physicians are:

- **Ejection fraction (EF)** or the fraction of blood that the left ventricle does pump out per beat.
- **Ventricular wall thickness** or the volume between both external and internal surfaces.

Those are currently derived from the 2D images.

### 3. DYNAMICAL EVOLUTION

The dynamic evolution of the model is based on Newtonian classic mechanics:

$$F_i = m_i \cdot \ddot{x}_i \begin{cases} \dot{x} = v \\ \dot{v} = F_i/m_i \end{cases}$$

Figure 3: Newtonian dynamics.

In figure 3, the mass is adjusted for every particle and the forces are defined as internal and external.

In order to solve the system, we need a numerical method. This method or solver, depends on the deformable model applied. We have used:

- Implicit Euler's method when using the plane deformable model.
- Explicit methods like Euler, Midpoint or Runge-Kutta-4 when using the spring-mass, restricted spring-mass and free deformation models.

Reports on these can be found at [Amatller00], [García00] and [Susin01].

### 4. INTERNAL FORCES

Internal forces define four possibilities for the model:

- *Plane deformation model*, where each of the triangles in the mesh has its own elasticity forces. Deformation will be characterized by the added action of three forces: stretch, shear and bend.
- *Spring-mass deformation model*, where the only internal force is stretch, defined between pairs of particles following Hook's equation.
- *Restricted spring-mass deformation model*, where spring-forces are only allowed in the normal direction of the derived vector field.
- *Free deformation model*, where the only existing force is the external one, derived from the data set. There's no connectivity between particles and topology must be maintained using a smoothing algorithm, apart from the evolution scheme.

All the models have been extensively reported in [Amatller00], [García00] and [Susin01]. The smoothing algorithm can be found at [García02].

### 5. EXTERNAL FORCES

External forces consist on the minimization of a functional that mixes the information derived from the image-intensities gradient with a diffusion term that allows the field to be spread out.

The vector field that acts as the external force is obtained then by minimizing the functional of figure 2.

$$\mathcal{E} = \iiint \mu \sum_{i \in \{x,y,z\}} (u_i^2 + v_i^2 + w_i^2) + |\nabla I|^2 |V - \nabla I|^2 dx dy dz$$

Figure 2: The energy-based functional.

This functional consists on two well-differentiated terms. On the left, the diffusion term that spreads the field when variations on intensities are negligible. On the right the property term, that dominates the expression when variations are important. The  $\mu$  parameter will control the balance between both terms.

Details on its implementation can be found at [Xu97][Xu98].

### 6. TEST MODEL: PHANTOM

In order to measure the reliability of the system from the results point of view, it becomes necessary to test a data set with known volume. The PHANTOM is a test-model that offers known geometry and volume, allowing us to compare with the obtained results. In our case we have used the one from the Vall d'Hebron Hospital which is presented in figure 4:

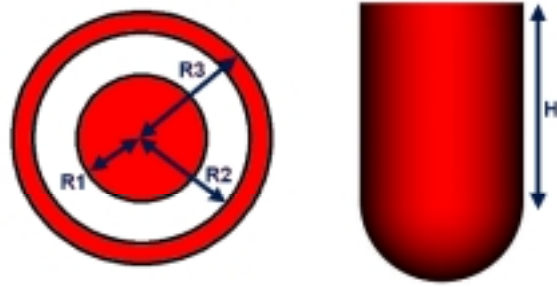


Figure 4: The PHANTOM dimensions.

With  $R1=20\text{mm}$ ,  $R2=35\text{mm}$ ,  $R3=45\text{mm}$  and  $H=55\text{mm}$ . Those distances give external and internal volumes of  $305301.4 \text{ mm}^3$  and  $89794 \text{ mm}^3$  respectively.

### 7. RESULTS

#### 7.1 Oscillations

If we analyse several particles trajectories:

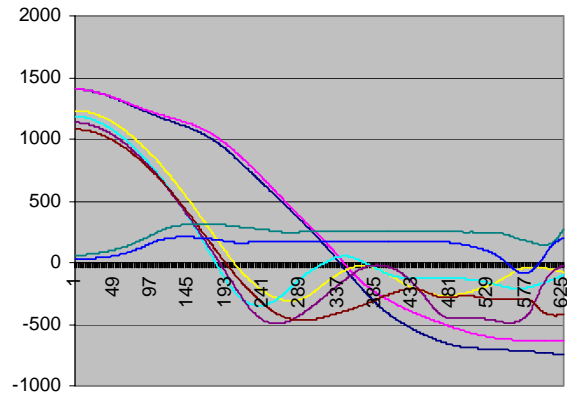
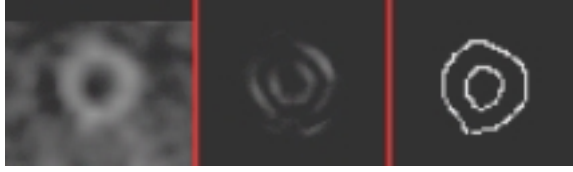


Figure 5: Particles oscillate in data frontiers.

We can see the oscillation effect in the frontiers of the data. Figure 5 shows the distance between several particles and the data to be recovered. Defining the black line (0) as the zero-distance to data, it becomes clear that particles oscillate while the system iterates, even if they have reached the surroundings of the data frontiers.

This behaviour demands for a stopping mechanism that we have implemented by using an accurate segmentation filter: the *Canny-Edge Detector* [Canny86], in order to mark the border voxels (data frontiers).



**Figure 6: Original SPECT image (left), after Reynolds operator (middle) and after Canny operator (right).**

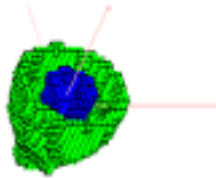
As figure 6 shows, an appropriate tuning of the filter (1.8 for the Gaussian, 0.3 for the low threshold and 0.8 for the high threshold) ensures performance for SPECT images rather than using less sophisticated operators like the Reynolds gradient.

After segmentation and determination of border voxels, it is necessary to separate them into internal and external. From the knowledge of the left ventricle's shape, we derived a radial-circumferences-based algorithm that can be stated as follows:

1. For each of the data slice.
2. Create an initial small centred circumference.
3. Increment diameter until finding first and/or second maximum number of border voxels.
4. If only one maximum is detected, mark these voxels as external.
5. Else mark first maximum as internal, second as external.

The algorithm relies on the effectiveness provided by the Canny-Edge Detector and the symmetry of the left-ventricle's images.

Figure 7 shows the internal and external frontiers detected for the PHANTOM test model.



**Figure 7: internal (blue) and external (green) frontiers for the PHANTOM data set.**

## 7.2 Distance to real data

We present a comparison between deformation models and final distance of the surface to data in table 1. Initial mesh consisted on 642 particles and 1280 triangles. We used a GVF balancing constant of 25.0 and a damping factor of 25%. K and KD stand for constant and damping constant respectively.

The implicit scheme (plane deformation) is clearly slower than the explicit one (spring-mass and free cases) but  $\Delta t$  can be bigger in the implicit methods. Despite we have used a smaller  $\Delta t$  for the explicit schemes they are faster even under those circumstances. The free model achieves

97% of the particles really close to data (less than one voxel) while the rest stays at the 75% approximately.

|             | Plane (1) | Plane (2) | Spring-Mass | Free      |
|-------------|-----------|-----------|-------------|-----------|
| $\Delta t$  | 0.01 s.   | 0.05 s.   | 0.0005 s.   | 0.0005 s. |
| % < 1 voxel | 77 %      | 74.5 %    | 73.6 %      | 97 %      |
| K Stretch   | 10        | 10        | 10          | ---       |
| KD Stretch  | 1         | 1         | 1           | ---       |
| K Bend      | 10        | 10        | ---         | ---       |
| KD Bend     | 1         | 1         | ---         | ---       |
| K Shear     | 1         | 1         | ---         | ---       |
| KD Shear    | 0.1       | 0.1       | ---         | ---       |

**Table 1: Final distances depending on the deformation model.**

Even being more controllable, the plane model is considerably slower and difficult to parameterise. With simple models and using explicit schemes we can reach faster and sufficiently precise solutions for our problem.

## 7.3 Size of triangles

The final 3D model will consist both on surface and on internal volume. It will be necessary to perform a tetrahedralization between both surfaces, external and internal. This process, which will be a further step in our project, will permit the real-time interaction with the synthetic organ. Tetrahedralization will associate internal triangles with its external neighbours. Then it is imperative to ensure final quality of the mesh, rejecting all possible degenerations.

A detailed mesh will recover data with minimal error but won't be smooth enough. On the contrary, if the initial triangle size is greater or equal than the separation between data slices, we can ensure a good aspect ratio for the triangles (area / major edge).

The initial mesh is created from a sphere centred at the origin. We evaluate the mass-centre for the data and its bounding box. Those properties allow us to scale and translate the sphere in order to begin the simulation not far from the data.







Table 2 depicts the evaluated meshes:

|           | 1             | 2            | 3           |
|-----------|---------------|--------------|-------------|
| Meshes    |               |              |             |
| particles | 162           | 642          | 2562        |
| triangles | 320           | 1280         | 5120        |
| Averaged  | 133.38 / 6.95 | 33.82 / 3.49 | 8.48 / 1.75 |
| Max       | 183.87 / 8.28 | 47.85 / 3.96 | 12.2 / 1.99 |
| Min       | 111.8 / 6.25  | 28.18 / 3.12 | 7.05 / 1.55 |

**Table 2: Initial meshes (mm<sup>2</sup>/normalized).**

We can see that triangles in mesh 1 are considerably bigger than in the rest. None of the meshes present degenerations. The amount of triangles is static and won't

be altered during the simulation that will be performed using the free-model approach.

|   | Flat shading  | Gouraud shading   | Averaged    | Max           | Min             |
|---|---|---|-------------|---------------|-----------------|
| 1 |  |  | 84.03 / 5.1 | 170.02 / 7.73 | 23.15 / 1.99    |
| 2 |  |  | 22.5 / 2.57 | 116.4 / 5.24  | 0.82 / 0.09     |
| 3 |  |  | 6.24 / 1.29 | 72.38 / 4.95  | 0.0007 / 0.0005 |

**Table 3: Reconstructions depending on the LoD of the meshes.**

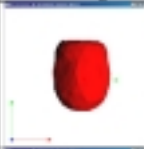

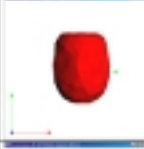
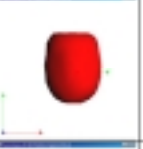
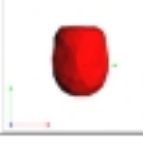
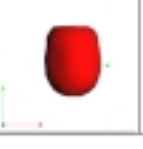
Table 3 shows the recovered PHANTOM using the three meshes. First case does not present any degenerations. However minimal area has changed notably its value. Second case starts some troubles, dealing with degenerations as we can derive from its minimal area value. Third case presents clear degeneration problems.

We conclude that the first mesh, where triangle dimensions are similar to space between data-slices, is smooth enough and gives not degenerations.

#### 7.4 Volume estimation

Volume results are presented comparing the real data volume with the one reconstructed. We compute the real volume by filtering data voxels, rejecting those with intensities lower than 20% of the maximum.

If we quantify the data volume we obtain a value of 368782 mm<sup>3</sup>. This volume differs from the theoretical one in a 12%. We must take in account the low resolution of the data and the error due to the quality of the reception from the medical equipment.

| Flat shading  | Gouraud shading   | Error (%) | $\Delta T$ (s) | Time (s) | Solver    |
|---|---|-----------|----------------|----------|-----------|
|  |  | 1.44      | 0.1            | 0.322    | Euler     |
|  |  | 0.68      | 0.12           | 0.14     | Mid Point |
|  |  | 1.53      | 0.17           | 0.111    | RK4       |

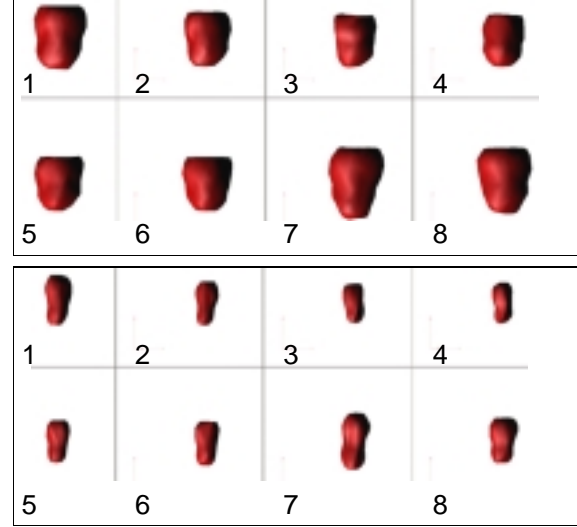
**Table 4: Volume results vs. numerical method.**

The simulations presented on table 4 have been executed using the free deformation method with the smoothing algorithm active. The selected initial mesh is the one

labelled as 2 in table 2. From top to bottom simulations were performed using the Euler, Midpoint and Runge-Kutta-4 methods. The third column shows the computed % of error between the recovered and the real data. All three numerical schemes are satisfactory in the sense that achieve errors less than 2%.

#### 7.5 A complete cardiac cycle reconstruction

Figure 8 presents a complete cardiac cycle, recovered from actual patient's data:



**Figure 8: Complete cardiac cycle with external surfaces (top) and internal surfaces (bottom).**

The cycle is formed by eight temporal acquisitions. Each data set consists on 64 x 64 x 24 voxels, with spatial resolutions of 2.87 mm (X), 2.87 mm (Y) and 5.74 mm (Z).

The meshes were generated using the free deformation model with the RK4 explicit scheme, using a GVF balancing constant of 10, a damping factor of 1% and a time increment  $\Delta t$  of 0.1 seconds.

One can observe the changes in volume as the organ beats, here noticeable as the sequence defines a complete cardiac cycle.

Internal mesh, external mesh and wall volumes (mm<sup>3</sup>) are presented in table 5:

|             | 1      | 2      | 3      | 4      |
|-------------|--------|--------|--------|--------|
| <b>Int.</b> | 74741  | 45677  | 36523  | 32956  |
| <b>Ext.</b> | 443762 | 316804 | 254112 | 250131 |
| <b>Wall</b> | 369021 | 271127 | 217589 | 217175 |
|             | 5      | 6      | 7      | 8      |
| <b>Int.</b> | 47237  | 55825  | 79581  | 63133  |
| <b>Ext.</b> | 299779 | 345830 | 473608 | 451525 |
| <b>Wall</b> | 252542 | 290005 | 394027 | 388392 |

**Table 5: Volumes for the eight temporal instances.**

Then EF can be calculated for this ventricle as it is shown in figure 9.

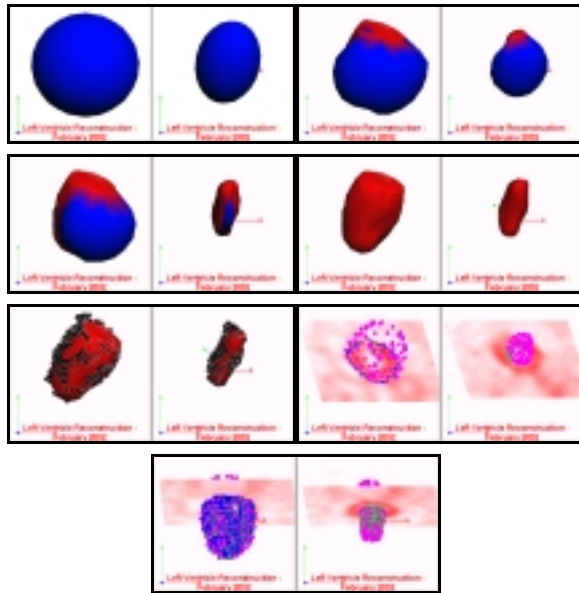
$$EF = \frac{DiastoleEndVolume - SystoleEndVolume}{DiastoleEndVolume}$$

$$= \frac{79581 - 32956}{79581} = 0.586 \Rightarrow 58.6\%$$

**Figure 9: EF calculation equation.**

Where all the volumes are internal. As it is showed, EF value is inside the interval 50% - 70% which states for a non-pathological situation.

Figure 10 shows the complete process for a reconstruction, in this case the first data set of the cycle. Both, the external (left) and internal (right) surface organ are recovered starting with the initial bounding ellipsoid :



**Figure 10: A complete reconstruction process.**

The sequence shows the initial meshes in blue. As mentioned before, those consist on scaled-translated spheres. The reconstruction begins and the meshes turn red as long as the particles reach the marked voxels borders. Finally the figure shows the border voxels (black) superimposed to meshes, the particles over a data slice, and some particles over the external (blue) and internal (green) frontiers.

### 7.6 Reconstructions with missing-data

When a patient has had a heart attack some of the areas of his heart becomes ischemic and, because of the absence of blood irrigation, the data we obtain can have some missing zones. Evaluating recovering results with partial missing data require using different fillings of the PHANTOM volume. We made some recovering test experiments with 10%, 32% and 53% percentages of missing volume data, always referred to the 100% of the total.

In these test, a different PHANTOM model (more geometric heart-like) was used. Its volume was 265501 mm<sup>3</sup>.

Table 6 shows the final results:

|  |   |
|--|---|
|  | Volume=265501 mm <sup>3</sup><br>% of total=100%  |
|  | Volume=250944 mm <sup>3</sup><br>% of total=94.5% |
|  | Volume=188360 mm <sup>3</sup><br>% of total=70.9% |
|  | Volume=159970 mm <sup>3</sup><br>% of total=60.2% |

**Table 6: Recovered surfaces from partial data.**

Here the first column shows the initial data to be recovered, the second column depicts the final meshes and the third column points out the recovered final volumes (absolute values and percentage of total).

As we can see, the best recovering is the third one because it gives a percentage of missing volume of 29.1% against the 32% of the real data emptied. This represents a relative percentage error of 0.09. For the other test examples we obtain relative errors of 0.45 and 0.24 respectively.

## 8. CONCLUSIONS

We have presented the results obtained until now with the SPECT data we are dealing. In terms of precision, computing time and model accuracy different strategies have been tested.

The whole process we are using can be described as:

1. Every image center and the useful slices are marked manually.
2. User specifies a filtering circle as a first noise-elimination tool. Outside data is rejected.
3. Voxels data are built from images and filtered using the Canny Edge Detector.
4. Identification of external and internal borders.
5. Computation of the associated GVF vector fields.
6. Reconstruction of external and internal surfaces, for each instant time, using the free deformation model, the RK4 numerical scheme and the smoothing algorithm.

The final result is accurate enough for the usual medical practice. A compromise between speed and precision has to be assumed. In our present situation, we have decided to use the fastest method after testing the other approaches and checking that acceptable precision is achieved. As a function of the final application other strategies can be chosen.

## 9. FUTURE WORK

The complete process is well-oriented but not finished. In order to improve the results, several goals must be reached:

- Establishing the definitive stopping mechanism.
- Detecting the frontiers suitably in all the pathological cases (missing data).
- Defining the optimal correspondence for the registration process in the whole cardiac cycle.
- Enhancing the numerical efficiency.

This work is also a piece of a bigger project where a 3D volume model will be constructed allowing the users to manipulate it in a virtual environment.

## 10. ACKNOWLEDGEMENTS

The authors wish to thank all the members of the medical applications research group at the IRI-UPC, the Nuclear Cardiology team at Vall d'Hebrón Hospitals and the people integrating the graphics & VR group at the CITeM.

This work has been partially financed by a TIC2000-1009 CYCIT project. The first author is granted by an EPSON "Rosina Ribalta" prize.

## 11. REFERENCES

- [Amatller00] J. Amatller, O. García, A. Susín. "Modelo Dinámico para la segmentación automática de imágenes 3D", X Congreso Español de Informática Gráfica-CEIG'2000, pág. 355-370, Junio 2000.
- [Bro-Nielsen94] Morten Bro-Nielsen: "Active Nets and Cubes", IMM Tech. Rep 94-13, 1994.
- [Canny86] J. Canny. "A Computational Approach to Edge Detection", IEEE Transactions on Pattern Analysis and Machine Intelligence, Vol. 8, No. 6, Nov. 1986.
- [Cohen93] L. D. Cohen and I. Cohen, "Finite-Element Methods for Active Contour Models and Balloons for 2-D and 3-D", IEEE Transactions. PAMI, vol. 15, no. 11, pag. 1131-1147, 1993.
- [García00] O. García, A. Susín, I. Navazo. "Segmentación Automática mediante un modelo dinámico. Aplicación a la reconstrucción del ventrículo izquierdo", Jornadas de Investigación en Ingeniería Biomédica, Sitges, 2-3 Noviembre 2000.
- [García02] O. García i Panyella. "Diploma d'Estudis Avançats", Escola Tècnica Superior d'Enginyeria Electrònica i Informàtica La Salle, Universitat Ramon Llull. Març 2002.
- [Kass88] M. Kass, A. Witkin, and D. Terzopoulos, "Snakes: Active Contour Models", International Journal of Computer Vision, vol. 1, no. 4, pag. 321-331, 1988.

[Lorensen87] W. Lorensen and H. Cline, "Marching Cubes: A High Resolution 3D Surface Construction Algorithm", Proceedings. SIGGRAPH'87, pag. 163-169, 1987.

[Mannting95] Finn Mannting, Puneet K Chandak, Yanina V Zabrodina, B Leonard Holman, "Atlas of Myocardial Perfusion SPECT", Brigham and Women's Hospital, Harvard Medical School, Boston MA. 1995-1997.

On-line atlas available at:

<<http://brighamrad.harvard.edu/education/online/Cardiac/Cardiac.html>>

[McInerney94] T. McInerney and D. Terzopoulos, "A Dynamic Finite Element Surface Model for Segmentation and Tracking in Multidimensional Medical Images with Application to Cardiac 4D Image Analysis", Journal of Computerized Medical Imaging and Graphics, 1994.

[Quackenbush96] D. Quackenbush, P. Ratiu, and J. Kerr, "Segmentation of the Visible Human Data Set", The Visible Human Project Conference, pag. 69-70, 1996.

[Sakaue96] K. Sakaue, "Stereo Matching by the Combination of Genetic Algorithm and Active Net", Systems and Computers in Japan, vol. 27, no. 1, pag. 40-48, 1996.

[Susin01] A. Susín, O. García. "Modelo dinámico para la reconstrucción del corazón humano", CEDYA 2001, XVII Congreso de Ecuaciones Diferenciales y Aplicaciones y VII Congreso de Matemática Aplicada, Universidad de Salamanca, 24-28 de Septiembre de 2001.

[Takanashi98] I. Takanashi, S. Muraki, A. Doi, and A. Kaufman, "3D Active Net for Volume Extraction", Proc. SPIE Vol. 3298, p. 184-193, Visual Data Exploration and Analysis V, Robert F. Erbacher; Alex Pang; Eds. 5/1998

[Xu97] C. Xu and J.L. Prince, "Gradient Vector Flow: A New External Force for Snakes", IEEE Proc. CVPR, 1997.

[Xu98] C. Xu and J.L. Prince, "Snakes, Shapes, and Gradient Vector Flow", IEEE Transactions on Image Processing, pag. 359-369, 1998.